

Observation of interference between two molecular Bose-Einstein condensates

C Kohstall^{1,2}, S Riedl^{1,2}§, E R Sánchez Guajardo^{1,2},
L Sidorenkov^{1,2}, J Hecker Denschlag¹||, and R Grimm^{1,2}

¹ Institut für Experimentalphysik und Zentrum für Quantenphysik, Universität Innsbruck, 6020 Innsbruck, Austria

² Institut für Quantenoptik und Quanteninformation, Österreichische Akademie der Wissenschaften, 6020 Innsbruck, Austria

Abstract. We have observed interference between two Bose-Einstein condensates of weakly bound Feshbach molecules of fermionic ^6Li atoms. Two condensates are prepared in a double-well trap and, after release from this trap, overlap in expansion. We detect a clear interference pattern that unambiguously demonstrates the de Broglie wavelength of molecules. We verify that only the condensate fraction shows interference. For increasing interaction strength, the pattern vanishes because elastic collisions during overlap remove particles from the condensate wave function. For strong interaction the condensates do not penetrate each other as they collide hydrodynamically.

§ Present address: Max-Planck-Institut für Quantenoptik, Garching, Germany.

|| Present address: Institut für Quantenmaterie, Universität Ulm, Germany.

1. Introduction

Interference manifests the wave nature of matter. The concept of matter waves was proposed by de Broglie in 1923 [1] and now represents a cornerstone of quantum physics. Already in the 1920's, experiments demonstrated the diffraction of electrons [2] and of atoms and molecules [3]. These early achievements led to the field of atom optics and interferometry [4–6].

With the realization of Bose-Einstein condensates (BECs) [7–9], sources of macroscopically coherent matter waves became available. The interference between two BECs was first observed by Andrews et al. [10]. This landmark experiment evidenced interference between two independent sources and revealed the relative phase between them [11]. Since then, interference measurements have developed into an indispensable tool for research on BEC. Applications include detection of the phase of a condensate in expansion [12], investigation of a condensate with vortices [13], and studies of quasi-condensates [14] or Luttinger liquids [15] in reduced dimensions. Another fundamental line of research in matter-wave optics is to explore the transition from the quantum to the classical world by detecting the wave nature of progressively larger particles, like clusters [16], C_{60} [17], and other giant molecules [18].

The creation of molecular Bose-Einstein condensates (mBECs) of paired fermionic atoms [19–21] provides us with macroscopically coherent molecular matter waves. In this article, we present the interference of two such mBECs and demonstrate interference as a tool to investigate condensates of atom pairs. This work extends the interference of condensates towards larger, composite particles.

In a Young-type interference experiment, we release two mBECs from a double-well trap and, after the condensates have overlapped, we observe an interference pattern by absorption imaging. In Sec. 2, we describe the experimental procedures in detail. In Sec. 3, we present our main experimental results, demonstrating the *molecular* de Broglie wavelength and the dependence of the interference contrast on temperature and interaction strength. Increasing the interaction strength reduces the visibility because of increasing elastic scattering losses depleting the coherent matter wave. Section 4 gives an outlook to possible extensions and applications of interference of pair condensates.

2. Experimental procedures

2.1. Preparation of the molecular Bose-Einstein condensate

We create a molecular Bose-Einstein condensate (mBEC), starting from an atomic Fermi gas consisting of an equal mixture of ${}^6\text{Li}$ in the lowest two spin states. The preparation follows the procedures described in our previous work [19, 22–24].

The atoms are trapped in the potential of a focused, far red-detuned laser beam with a beam waist of $45\ \mu\text{m}$, derived from a 25 W, 1030 nm single-mode laser source, as illustrated in Fig. 1. We choose the coordinate system such that the laser beam

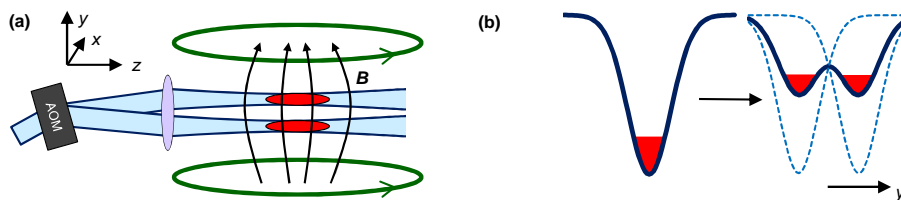


Figure 1. Illustration of the trapping and splitting of the mBEC in the presence of a magnetic field B . An acousto-optical modulator (AOM) toggles the laser beam between two positions, which creates an effective double-well potential for trapping two mBECs. (a) Along the x - and y -directions, the optical potential is dominant; along the z -axis the magnetic potential is dominant. (b) The potential shape of the optical dipole trap is Gaussian. The double-well potential is generated from the superposition of two Gaussian potentials.

propagates along the z -axis and gravity acts in $-y$ -direction. A magnetic bias field B can be applied along the y -axis. A broad Feshbach resonance centered at $B = 834$ G [25] facilitates precise tuning of the atomic s -wave scattering length a . Below resonance, a weakly bound molecular state exists [26]. Molecules in this state represent halo dimers, since their wave function extends far into the classically forbidden range [27]. Their size is given by a and their binding energy is $\hbar^2/(ma^2)$, where m denotes the atomic mass and \hbar is Planck's constant h divided by 2π . The intermolecular scattering length is $a_M = 0.6a$ [28].

To create the mBEC we perform evaporative cooling by reducing the laser beam power at a constant magnetic field $B = 764$ G. During evaporation, the halo dimers are created through three-body collisions [19] and eventually they form a mBEC [29]. After evaporation, we increase the trap depth, thereby compressing the condensate, to avoid spilling particles in all further steps of the experimental sequence. The beam power is adiabatically increased by a factor of about 10 to 45 mW. The trap center can be closely approximated by a harmonic potential. The oscillation frequencies of the molecules, which are the same as the ones of free atoms, are $(\omega_x, \omega_y, \omega_z) = 2\pi \times (250, 250, 20.6 \times \sqrt{B/700 \text{ G}})$ Hz. The axial confinement essentially results from the curvature of the magnetic field. We obtain a cigar-shaped cloud containing $N = 1.8 \times 10^5$ molecules. The condensate fraction exceeds 90% [19].

Most of our measurements are carried out in the regime of weak interaction between the molecules. We ramp the magnetic field adiabatically down to 700 G in 200 ms, thereby decreasing the scattering length to about $a_M = 1000 a_0$; at lower fields the molecules become unstable [26, 30, 31] and limit the lifetime of the mBEC. At 700 G, the chemical potential of the mBEC is $k_B \times 200$ nK, with k_B denoting the Boltzmann constant, and the binding energy of the molecules is $k_B \times 8 \mu\text{K}$. In view of the crossover from BEC to a Bardeen-Cooper-Schrieffer (BCS) type regime [29, 32], one can also express the interaction conditions in terms of the commonly used dimensionless parameter $1/(k_F a)$, where k_F is the Fermi wave number of a non-interacting Fermi gas with $(\hbar k_F)^2/(2m) = E_F$, where $E_F = \hbar(6N\omega_x\omega_y\omega_z)^{1/3}$ is the Fermi energy. For the

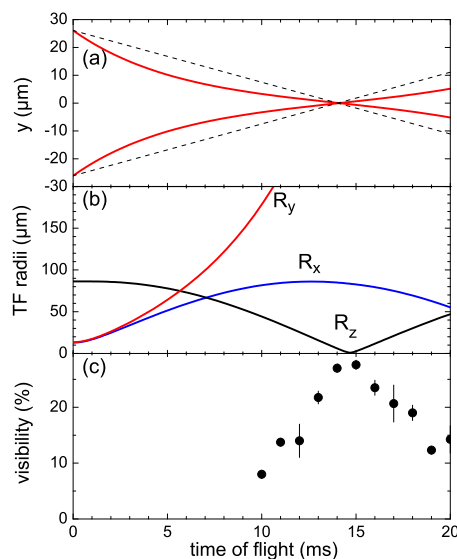


Figure 2. Expansion dynamics of the condensates in the magnetic saddle potential. (a) The solid lines are the calculated center-of-mass motion of the condensates, taking into account an initial kick towards each other, see text. The trajectories intersect after $t_{\text{TOF}} = 14$ ms. For comparison, the dashed lines represent the trajectories of particles in free expansion intersecting at the same point. (b) The calculated Thomas-Fermi radii of the condensates show the expansion along the x - and y -axis and the compression along the z -axis. The initially cigar-shaped mBEC evolves into a flat disc. (c) The measured visibility of the fringe pattern shows a clear peak, which coincides with the minimum in R_z . The bars indicate the statistical uncertainties derived from 10 individual measurements.

condition of our mBEC at 700 G we obtain $1/(k_F a) = 3$. Strongly interacting conditions are realized for $1/(k_F a) < 1$, which can be achieved at fields closer to resonance.

2.2. Condensate splitting

The mBEC is split into two equal parts along the y -axis. We transform the Gaussian shaped optical dipole potential into a double-well potential, as illustrated in Fig. 1(b). This is accomplished by using time-averaged potentials. An acousto-optical deflection system modulates the trapping beam position so fast that the atoms do not follow and feel the time-averaged beam intensity as their motional potential [33, 34]. The modulation frequency is 200 kHz and the trapping beam is toggled between two positions, the distance of which is increased from 0 to $68 \mu\text{m}$ within 50 ms. The distance between the minima of the resulting double well is somewhat smaller because the two Gaussian potentials still overlap. The measured distance between the centers of the two condensates is $s = 56 \mu\text{m}$ and the measured oscillation frequencies in each well are $(\omega_x, \omega_y, \omega_z) = 2\pi \times (164, 146, 20.6 \times \sqrt{B/700 \text{ G}})$ Hz. The chemical potential of both condensates is $k_B \times 100$ nK and the interaction parameter is $1/(k_F a) = 4$. The barrier height is $k_B \times 160$ nK, which leads to a fully negligible tunneling rate. The number ratio

between the two condensates after splitting is sensitive to imperfections of the optical potential. To control equal number splitting, we fine-tune the magnetic gradient field that is applied to compensate for the effect of gravity.

2.3. Expansion in the magnetic field

The specific expansion dynamics of the released mBECs in our setup is the key to making interference clearly observable, and the understanding of the expansion is essential for the interpretation of our results. We identify two effects, which result from the curvature of the magnetic field, that are favorable for the observation of interference.

The coils generating the magnetic offset field in our set-up are not in Helmholtz configuration, which leads to second-order terms in $B(x, y, z)$. The resulting magnetic potential is a saddle potential, where the molecules are trapped along the x - and z -directions, but they are anti-trapped along the y -axis, the symmetry axis of the field. The oscillation frequencies are $(\omega_x, \omega_y, \omega_z) = 2\pi \times (20.5, i \times 29, 20.5) \times \sqrt{B/700} \text{ GHz}$, where the imaginary frequency denotes the anti-trap along the y -axis.

We model the expansion by adopting the scaling approach as applied in Refs. [33, 35]. Figure 2(b) shows the predicted evolution of the Thomas-Fermi (TF) radii R_x , R_y and R_z , which we also verify experimentally. At the beginning, the expansion is driven by the pressure gradient in the cloud, which leads to a fast acceleration in the radial direction. This expansion is then further accelerated along y and decelerated along x because of the magnetic saddle potential. Along the z -axis, the long axis of the trapped cloud, the trap remains basically unchanged when the cloud is released from the optical potential. As the mean field pressure of the expanding cloud decreases, the magnetic confinement leads to a spatial compression of the cloud. We find that after $t_{\text{TOF}} \approx 14 \text{ ms}$ the parameter R_z has a minimum because of this compression effect.

For high interference contrast, large overlap of the two clouds at the time of detection is essential. To achieve this, the condensates are kicked towards each other by switching on the original single-well trap, typically for 0.1 ms right after release from the double well. The solid lines in Fig. 2(a) show the calculated center-of-mass motion of the clouds after the initial kick to assure large overlap at $t_{\text{TOF}} \approx 14 \text{ ms}$.

The interference pattern is determined by the relative velocity between the two condensates. The relative velocity v_{rel} at $y = 0$ and $t_{\text{TOF}} = 14 \text{ ms}$ can be directly deduced from the slopes of the solid lines in Fig. 2(a). This velocity is substantially smaller than it would be in free expansion without magnetic potential, where particles meeting at $y = 0$ and $t_{\text{TOF}} = 14 \text{ ms}$ would follow the dashed trajectories in Fig. 2(a). This deceleration of v_{rel} can be readily visualized by the condensates climbing up the potential hill resulting from the anti-trap in y -direction. This anti-trap also accelerates the expansion in y -direction, see R_y in Fig. 2(b). Remarkably, since the velocity field in each of the clouds stays linear, v_{rel} is independent of the position. More rigorously, we calculate v_{rel} using the scaling approach and taking into account the center-of-mass motion of the clouds.

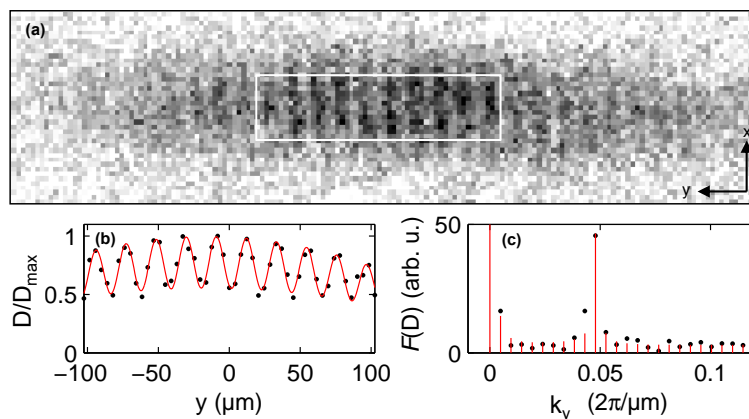


Figure 3. Interference image and analysis. (a) The column density along the z -axis after $t_{\text{TOF}} = 14\text{ms}$ shows the interference pattern. The field-of-view is $660\ \mu\text{m} \times 170\ \mu\text{m}$. The inner box indicates the region used for analysis. (b) The column density integrated along x gives the density distribution D along y (dots). The solid curve is the result of the fit in Fourier space, see text. (c) The density distribution is Fourier transformed (dots) and fitted (bars).

Thus expansion dynamics brings about two favorable effects: First, the spatial compression along the z -axis facilitates clear detection of interference fringes by absorption imaging. Second, the decreased relative velocity leads to an increased fringe period. This means that the anti-trap acts as a magnifying glass for the interference fringes.

2.4. Detection and analysis of interference fringes

We detect the clouds by absorption imaging. Figure 3(a) shows a typical image of interference after 14 ms time of flight. The imaging beam propagates along the z -axis. It is overlapped with the trapping beam using dichroic mirrors. The imaging light pulse is on for $10\ \mu\text{s}$ and its intensity is about the saturation intensity of ${}^6\text{Li}$ atoms. We state-selectively image the atoms in the second-to-lowest Zeeman state. Already the first photon scattering event is likely to dissociate the weakly bound molecule [22], followed by about 10 more photons scattered by the free atom.

From the absorption images, we determine the visibility and fringe period of the interference pattern. The column density is integrated along the x -direction over the region depicted in Fig. 3(a) ¶ resulting in a one-dimensional density distribution D , shown in Fig. 3(b). The density distribution contains various kinds of noise (e.g. photon or atom shot noise, or camera readout noise), which may be misinterpreted as interference signal. Therefore we analyze the density distribution in Fourier space by considering the Fourier transformed density distribution $\mathcal{F}(D)$, see Fig. 3(c). Here all those types of noise are approximately white and show up as a constant offset, whereas,

¶ The size of the region was chosen to produce the optimal signal to noise.

the signal of interference is monochromatic and shows up as a peak. This gives the possibility to subtract the average contribution of noise from the signal. We determine the visibility and fringe period by the custom fit function in Fourier space

$$f = \sqrt{|\mathcal{F}((a + b y + c y^2) \times (1 + v \sin(2\pi/d y + \phi)))|^2 + n^2}, \quad (1)$$

yielding the fringe period d , the visibility v , and the relative phase ϕ . The term $a + b y + c y^2$ account for the somewhat non-uniform density distribution. The white noise n is the offset in Fourier space. Since the phase between the signal and the noise is random, the corresponding contributions are added quadratically. The discrimination of the noise via this fitting routine is crucial when the visibility is low.

The largest observed visibility is about 30%. We find that this upper limit can be essentially attributed to the finite resolution of our imaging system. We determine the modulation transfer function of the imaging system and it gives about $30 \pm 10\%$ visibility for structures with period $d = 20 \mu\text{m}$. Also other sources can contribute to a reduction of visibility, like a blurring because of a limited depth of focus or a tilt of the planes of constructive and destructive interference. The planes are in general somewhat tilted with respect to the line of sight, thereby obscuring the fringe pattern on the image. But these effects are suppressed by the spatial compression along the imaging axis caused by the magnetic saddle potential. This can be seen by comparing the compression of R_z in Fig. 2(b) to the detected visibility in Fig. 2(c). The minimum of R_z after $t_{\text{TOF}} = 14 \text{ ms}$ coincides with the peak in visibility. The peak value of almost 30% agrees with the resolution limit of the imaging system. All following measurements are performed when the clouds are compressed to about $1 \mu\text{m}$ along the imaging axis; in this case, only the limited resolution is relevant. The spatial compression is an alternative to the slicing imaging technique used in Ref. [10] and brings along the advantage that all particles are imaged.

3. Experimental results

The observed interference pattern is the standing wave formed by two macroscopically occupied matter waves, the two molecular BECs. Here we present our main experimental results. In Sec. 3.1, we investigate the fringe period, which evidences that the interfering particles are molecules. In Sec. 3.2, we study the visibility when heating the cloud to above the critical temperature for condensation to show that the interference is established by the condensate fraction. In Sec. 3.3, we explore the dependence of the visibility on the interaction strength and find that non-forward scattering processes depopulate the momentum component of the matter wave that is responsible for the interference pattern.

3.1. Fringe period

The fringe period is an central observable in interference experiments. Figure 4 shows the measured fringe period at $B = 700 \text{ G}$ as a function of time of flight. The de Broglie

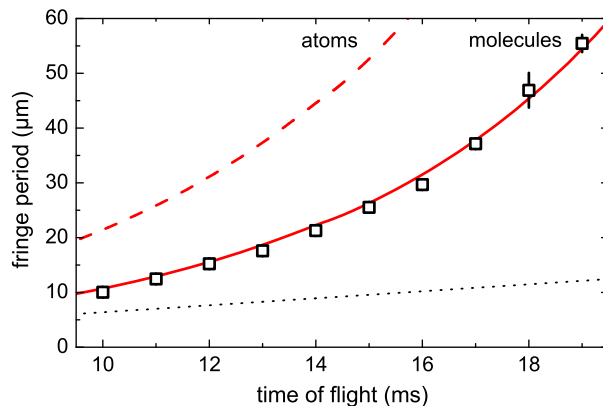


Figure 4. Fringe period as a function of time of flight. The symbols are the measured periods with bars, mostly smaller than the symbol size, indicating the statistical uncertainties resulting from 10 individual measurements at a given time of flight. The solid line is the calculated period for molecules and the dashed line for atoms. For free expansion without the magnetic saddle potential, the fringe period of molecules would be much smaller (dotted line).

relation yields the fringe period

$$d = \frac{h}{Mv_{\text{rel}}}, \quad (2)$$

which is determined by the mass M of the interfering particles and by the relative velocity v_{rel} of the two condensates. In our experiment, we calculate v_{rel} from the expansion and center-of-mass motion of the condensates in the magnetic field curvature, as discussed in Sec. 2.3. The result is in contrast to the simple relation $v_{\text{rel}} = s/t_{\text{TOF}}$ that holds for the free expansion usually considered in experiments of this type. The solid line in Fig. 4 displays the calculated fringe period d for molecules, where we set $M = 2m$. All input parameters for this calculation are determined independently. Their combined uncertainties result in typical uncertainty of 3% for the fringe period, with the main contribution stemming from the uncertainty in the cloud separation. The data are in remarkable agreement with the calculation. For comparison, we also plot the fringe period for interfering atoms ($M = m$), which is clearly incompatible with the data.

The dotted line in Fig. 4 displays the fringe period that would result for freely expanding mBECs without the magnetic saddle potential. Comparing this curve to the much larger fringe period that we observe, highlights the effect of the magnetic field curvature to magnify the fringe period, as discussed in Sec. 2.3. The same magnification effect was reported in Ref. [36].

Note that the fringe period can be increased by interaction-induced slowing down of the two overlapping condensates [12]. The mean-field of one condensate represents a potential hill for the other condensate, which slows down when climbing this hill. Under our experimental conditions at 700 G, the effect is found to be negligible. For stronger interaction, we see indications of this effect in agreement with a corresponding model calculations.

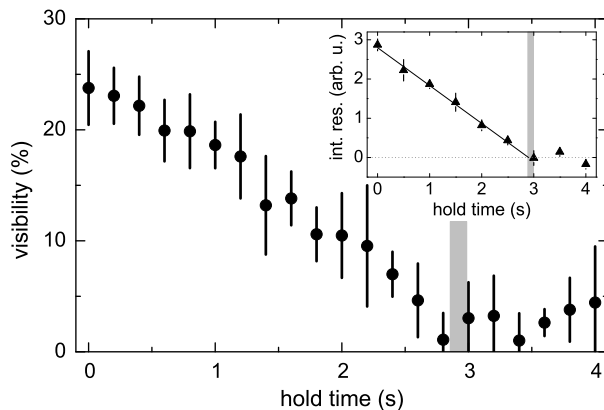


Figure 5. Visibility of interference for increasing temperature. The main figure shows the measured mean visibility with bars indicating the standard deviation resulting from 11 measurements. Here, we plot the standard deviation and not the statistical uncertainty to better illustrate the range of measured values. During the hold time in the trap, the temperature increases from low temperature to above T_c . The hold time after which T_c is reached is indicated by the grey bar. The inset shows the integrated residuals of a Gaussian fit, see text. A linear fit to the first six points facilitates a simple extrapolation to zero, which marks the vanishing of the condensate fraction.

3.2. Dependence of interference visibility on condensate fraction

To demonstrate that the interference results only from the condensed molecules and not from the thermal fraction, we perform a controlled heating experiment and show the loss of visibility with vanishing condensate fraction. Starting from an almost pure condensate [19], we hold the gas in the recompressed optical dipole trap for a variable hold time before splitting. Intensity fluctuations and pointing instabilities of the laser beam as well as inelastic collisions between the molecules [30] heat the gas and lead to a monotonous temperature increase [37,38]. To demonstrate that the interference results from the condensate, it is sufficient to determine the hold time at which the critical temperature for condensation T_c is reached. Therefore, we fit a Gaussian profile to the density distribution of the cloud, which is recorded after expansion for $t_{\text{TOF}} = 5$ ms from the single-well trap. We find that the integrated residual of the fit gives a good measure whether the cloud shape deviates from a thermal one. The inset in Fig. 5 shows that the integrated residual goes to zero after a hold time slightly below 3s, which locates the phase transition.

The visibility data in Fig. 5 are recorded at $B = 700$ G after $t_{\text{TOF}} = 14$ ms⁺. The visibility decreases as the temperature increases and vanishes for a hold time that coincides with the hold time when T_c is reached. The observed decrease of visibility is continuous because we image the full column density including the growing thermal fraction, which does not clearly separate from the condensate in expansion at 700 G.

⁺ We verify on images after $t_{\text{TOF}} = 0.4$ ms that the clouds are still separated in the double-well potential despite the higher thermal energies.

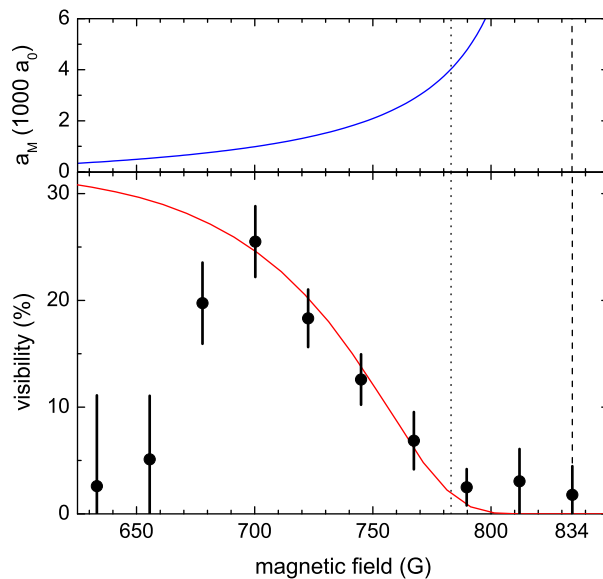


Figure 6. Visibility of interference from weak to strong interaction. The upper panel shows how the molecular scattering length a_M increases towards the Feshbach resonance at 834 G, marked by the dashed line. The onset of the strongly interacting regime is marked by the dotted line. In the lower panel, the dots represent the mean visibility with bars indicating the standard deviation resulting from 20 individual measurements. The solid line is the predicted visibility from the simple calculation modeling the non-forward scattering events.

Above T_c , the density distribution does no more show any fringes. Still, the fitting routine produces finite mean values because it can output only positive values. But if the measured visibility is not larger than the standard deviation, its distinction from zero is not significant. The vanishing visibility above the critical temperature confirms that, as expected, the interference is established by the condensate fraction.

Further intriguing evidence that the interference is caused by the condensate is the observation of interference between independent ultracold clouds. An independent production rules out that the interference can be caused by self interference of particles [39]. To investigate interference between independent clouds, we split them already at a temperature far above the critical temperature to a large distance of $180 \mu\text{m}$ and then create two mBECs independently. Shortly before release, we reduce the distance to obtain the identical geometry as in all the other measurements and proceed as usual. We observe the same kind of interference pattern with a visibility of about 15%. The lower visibility can be explained by a less efficient evaporation and less control over the equal number preparation in the double well.

3.3. Dependence of interference visibility on interaction strength

In a further set of measurements, we investigate how the fringe visibility depends on the interaction strength. Therefore we perform the interference experiment for different

magnetic field values, thereby changing the molecular scattering length a_M according to the upper panel of Fig. 6 *. The observed visibility as a function of the magnetic field is shown in the lower panel in Fig. 6. The highest visibility is found at about 700 G. For lower fields, the visibility is decreased, which we attribute to inelastic decay. The inelastic collisions of molecules lead to heating of the gas and loss of particles. The heating reduces the condensate fraction, which decreases the visibility as observed in the previous section. The loss also reduces the signal on the images. This leads to a higher statistical uncertainty in the determination of the visibility, showing up in the larger standard deviations below 700 G.

Towards larger interaction strength, our data show a pronounced decrease of visibility, and the visibility vanishes at about 780 G. This coincides with the onset of strong interaction in the trap, where $1/k_F a \approx 1$. We find that the main effect causing the decrease is elastic non-forward scattering. It is known from experimental and theoretical work on colliding condensates [40,41] that elastic non-forward scattering of particles removes them from the condensate wave function. In contrast to the forward scattering accounted for within the usual mean-field approach, this non-forward scattering transfers particles into momentum states of random direction, which therefore do no more contribute to the observed interference pattern. Non-forward scattering is a particle-like excitation, which requires v_{rel} to exceed the speed of sound v_s . The process is suppressed for smaller v_{rel} [40,42]. To estimate the decrease of visibility through this process, we perform a simple model calculation. The velocity dependence of non-forward scattering is included by the following approximation: no suppression for $v_{\text{rel}} \geq v_s$ and full suppression otherwise. We calculate the mean number of non-forward scattering events N_e for a representative molecule with molecules of the other condensate until the moment of detection. This representative molecule travels along the center-of-mass path of the condensate; see Fig. 2(a). We take the bosonically enhanced, unitarity limited scattering cross section $\sigma = 8\pi a_M^2 / (1 + (ka_M)^2)$, with $k = mv_{\text{rel}}/\hbar$. From N_e , we derive the probability for a molecule to still be part of the condensate. This probability is e^{-N_e} and directly corresponds to the expected visibility, which we fit to the data, excluding the three data points below 700 G. We obtain the solid line in Fig. 6. The only fit parameter is a normalization factor, which allows us to account for the reduced detected visibility because of the limited imaging resolution. The fit yields a factor of 0.32, which is consistent with the imaging resolution discussed in Sec. 2.4. We find that our simple model for non-forward scattering can very well explain the decrease of visibility towards high interaction strength.

There are also other effects that decrease the visibility for increasing interaction strength, but they turn out to be minor for our experimental conditions: Strong interaction lead to a depletion of the condensate [43]. Only the condensate contributes to the interference pattern and not the depleted fraction. The depleted fraction amounts to about 10 % at 780 G. As we expect the reduction of visibility to be proportional

* We verify on images after $t_{\text{TOF}} = 0.4$ ms that the clouds are still separated in the double-well potential despite the higher chemical potential at higher interaction strength.

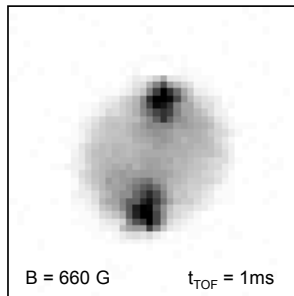


Figure 7. Absorption image 1 ms after the collision of two BECs. A spherical shell of scattered particles clearly separates from the two BECs. The field of view is $180 \times 180 \mu\text{m}$.

to the depletion, the reduction is negligible (at 780 G from 2.6% to 2.3%). Another effect reducing the visibility is the collisional dissociation of molecules during overlap. However, this effect can only occur above 800 G, where the collision energy exceeds the binding energy.

To directly demonstrate the effect of non-forward scattering, we study the collision of two condensates when their relative velocity v_{rel} is much faster than their expansion velocity. This allows us to observe the non-forward scattered particles in an s -wave shell [44], well separated from the condensates, see Figure 7. This separation was not present in the interference experiments reported before because v_{rel} was similar to the expansion velocity. We apply our simple model to calculate the fraction of non-forward scattered particles and find good agreement, confirming our model in an independent and direct way.

Close to the Feshbach resonance, we enter a regime where the number of collisions becomes large. This leads to hydrodynamic behavior also above T_c [38, 45]. The time of flight series in Fig. 8, taken on resonance, shows that the clouds do not penetrate each other in this regime. Instead, the flow of the particles is redirected into the x - z -plane leading to the observed high column density in the center. Unlike at low magnetic fields, the clouds do not superimpose. This directly excludes interference of two independent condensates in the strongly interacting regime. The scenario is similar to the one in Ref. [46] and may be described by the analysis therein.

The hindered overlap could be overcome by a magnetic field ramp to weak interaction after release and before overlapping, as done for the detection of vortices in Ref. [47]. Like the observation of vortices, the observation of interference would evidence the coherence of the strongly interacting superfluids.

In further measurements, performed above the Feshbach resonance towards the BCS regime, we did not observe interference. To discuss possible reasons for the absence of interference fringes, let us first consider the effect of non-forward scattering on the visibility. As on the BEC side, this effect may hinder overlap and interference for $1/k_F a < -1$, i.e. below 910 G. However, we also have to consider that the pairs on the

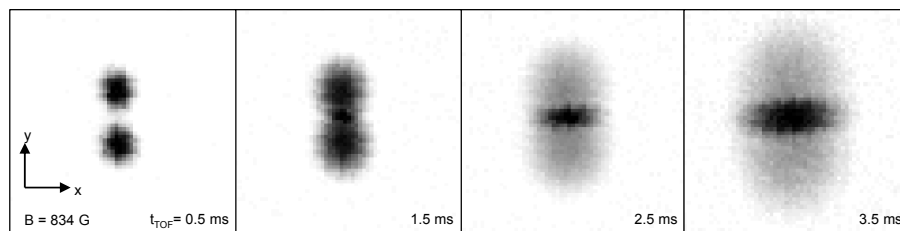


Figure 8. The hindered overlap on resonance. The series shows the first few milliseconds of expansion. The two clouds do not penetrate each other, but splash according to hydrodynamics. The field of view is $180 \times 180 \mu\text{m}$.

BCS side may not persist in expansion [48], unlike on resonance or on the BEC side. For the lowest achievable temperature in our experiment and at 910 G, the pairs would be already unstable after a very short expansion time according to Ref. [48].

4. Conclusion and outlook

In conclusion, we have observed the interference between two molecular BECs. The interference pattern visualizes the standing matter wave of the weakly bound Feshbach molecules and shows coherence over the spatial extension of the cloud. The contrast of interference vanishes above the critical temperature of condensation, demonstrating that the interference is established by the condensed molecules only. We find that non-forward elastic scattering processes can lead to a depletion of the condensate wave function while the clouds overlap. This effect increases towards higher interaction strength and prevents us from observing interference in the strongly interacting regime. On resonance we observe that the two clouds do not overlap but rather collide and deform as a result of deep hydrodynamic behavior.

Interference between condensates of paired fermionic atoms can serve as a powerful tool to investigate many exciting aspects of those systems. A future application will be given, for example, if p -wave condensates become available. Here, interference is predicted to reveal the vector nature of the order parameter [49]. A conceptually interesting regime will be entered when the size of the pairs becomes comparable to the fringe period. Then the detected distribution of atoms may not reveal the interference pattern of the pair distribution. Besides investigating condensates of paired fermions themselves, the system could be used to study the fundamental processes of interference. The wide tunability of the interaction strength could be used to assist self-interference [50] or to investigate to which extent interaction build up the observable relative phase [51].

Suppressing the effect of non-forward scattering during overlap could extend the range of applications of condensate interference. Such a suppression may be achieved by reducing the interaction strength before overlap using fast magnetic field ramping techniques [20, 47]. This technique would allow for investigating the interference in

the regime of strong interaction or even on the BCS side of the resonance, where the interference of Cooper-type pairs is an intriguing question in itself.

Acknowledgments

We thank Christopher Gaul for stimulating discussions. We acknowledge support by the Austrian Science Fund (FWF) within SFB 15 (project part 21) and SFB 40 (project part 4).

References

- [1] de Broglie L 1923 *Nature* **112** 540
- [2] Davisson C J and Germer L H 1927 *Nature* **119** 558-560
- [3] Estermann I and Stern O 1930 *Z. Phys.* **61** 95–125
- [4] Adams C S, Sigel M and Mlynek J 1994 *Physics Reports* **240** 143–210
- [5] Bongs K and Sengstock K 2004 *Reports on Progress in Physics* **67** 907
- [6] Cronin A D, Schmiedmayer J and Pritchard D E 2009 *Rev. Mod. Phys.* **81** 1051–1129
- [7] Anderson M H, Ensher J R, Matthews M R, Wieman C E and Cornell E A 1995 *Science* **269** 198–201
- [8] Davis K B, Mewes M O, Andrews M R, van Druten N J, Durfee D S, Kurn D M and Ketterle W 1995 *Phys. Rev. Lett.* **75** 3969–3973
- [9] Bradley C C, Sackett C A, Tollett J J and Hulet R G 1995 *Phys. Rev. Lett.* **75** 1687–1690
- [10] Andrews M R, Townsend C G, Miesner H J, Durfee D S, Kurn D M and Ketterle W 1997 *Science* **275** 637–641
- [11] Castin Y and Dalibard J 1997 *Phys. Rev. A* **55** 4330–4337
- [12] Simsarian J E, Denschlag J, Edwards M, Clark C W, Deng L, Hagley E W, Helmerson K, Rolston S L and Phillips W D 2000 *Phys. Rev. Lett.* **85** 2040–2043
- [13] Inouye S, Gupta S, Rosenband T, Chikkatur A P, Görlitz A, Gustavson T L, Leanhardt A E, Pritchard D E and Ketterle W 2001 *Phys. Rev. Lett.* **87** 080402
- [14] Hadzibabic Z, Kruger P, Cheneau M, Battelier B and Dalibard J 2006 *Nature* **441** 1118
- [15] Hofferberth S, Lesanovsky I, Fischer B, Schumm T and Schmiedmayer J 2007 *Nature* **449** 324
- [16] Schöllkopf W and Toennies J P 1994 *Science* **266** 1345–1348
- [17] Arndt M, Nairz O, Vos-Andreae J, Keller C, van der Zouw G and Zeilinger A 1999 *Nature* **401** 680–682
- [18] Gerlich S, Eibenberger S, Tomandl M, Nimmrichter S, Hornberger K, Fagan P J, Tüxen J, Mayor M and Arndt M 2011 *Nat. Commun.* **2** 263
- [19] Jochim S, Bartenstein M, Altmeyer A, Hendl G, Riedl S, Chin C, Hecker Denschlag J and Grimm R 2003 *Science* **302** 2101–2103
- [20] Greiner M, Regal C A and Jin D S 2003 *Nature* **426** 537–540
- [21] Zwierlein M W, Stan C A, Schunck C H, Raupach S M F, Gupta S, Hadzibabic Z and Ketterle W 2003 *Phys. Rev. Lett.* **91** 250401
- [22] Bartenstein M, Altmeyer A, Riedl S, Jochim S, Chin C, Hecker Denschlag J and Grimm R 2004 *Phys. Rev. Lett.* **92** 120401
- [23] Altmeyer A, Riedl S, Kohstall C, Wright M J, Geursen R, Bartenstein M, Chin C, Hecker Denschlag J and Grimm R 2007 *Phys. Rev. Lett.* **98** 040401
- [24] Riedl S, Sánchez Guajardo E R, Kohstall C, Altmeyer A, Wright M J, Hecker Denschlag J, Grimm R, Bruun G M and Smith H 2008 *Phys. Rev. A* **78** 053609
- [25] Bartenstein M, Altmeyer A, Riedl S, Geursen R, Jochim S, Chin C, Hecker Denschlag J, Grimm R, Simoni A, Tiesinga E, Williams C J and Julienne P S 2005 *Phys. Rev. Lett.* **94** 103201

- [26] Jochim S, Bartenstein M, Altmeyer A, Hendl G, Chin C, Hecker Denschlag J and Grimm R 2003 *Phys. Rev. Lett.* **91** 240402
- [27] Ferlaino F, Knoop S, Mark M, Berninger M, Schöbel H, Nägerl H C and Grimm R 2008 *Phys. Rev. Lett.* **101** 023201
- [28] Petrov D S, Salomon C and Shlyapnikov G V 2005 *Phys. Rev. A* **71** 012708
- [29] Inguscio M, Ketterle W and Salomon C (eds) 2008 *Ultra-cold Fermi Gases* (IOS Press, Amsterdam) Proceedings of the International School of Physics “Enrico Fermi”, Course CLXIV, Varenna, 20-30 June 2006
- [30] Petrov D S, Salomon C and Shlyapnikov G V 2005 *J. Phys. B: At. Mol. Opt. Phys.* **38** 645–660
- [31] Cubizolles J, Bourdel T, Kokkelmans S J J M F, Shlyapnikov G V and Salomon C 2003 *Phys. Rev. Lett.* **91** 240401
- [32] Giorgini S, Pitaevskii L P and Stringari S 2008 *Rev. Mod. Phys.* **80** 1215
- [33] Altmeyer A, Riedl S, Wright M J, Kohstall C, Denschlag J H and Grimm R 2007 *Phys. Rev. A* **76** 033610
- [34] Shin Y, Saba M, Pasquini T A, Ketterle W, Pritchard D E and Leanhardt A E 2004 *Phys. Rev. Lett.* **92** 050405
- [35] Menotti C, Pedri P and Stringari S 2002 *Phys. Rev. Lett.* **89** 250402
- [36] Zawadzki M E, Griffin P F, Riis E and Arnold A S 2010 *Phys. Rev. A* **81** 043608
- [37] Savard T A, O’Hara K M and Thomas J E 1997 *Phys. Rev. A* **56** R1095–R1098
- [38] Wright M J, Riedl S, Altmeyer A, Kohstall C, Guajardo E R S, Denschlag J H and Grimm R 2007 *Phys. Rev. Lett.* **99** 150403
- [39] Miller D E, Anglin J R, Abo-Shaeer J R, Xu K, Chin J K and Ketterle W 2005 *Phys. Rev. A* **71** 043615
- [40] Chikkatur A P, Görlitz A, Stamper-Kurn D M, Inouye S, Gupta S and Ketterle W 2000 *Phys. Rev. Lett.* **85** 483–486
- [41] Band Y B, Trippenbach M, Burke J P and Julienne P S 2000 *Phys. Rev. Lett.* **84** 5462–5465
- [42] Band Y B, Burke J P, Simoni A and Julienne P S 2001 *Phys. Rev. A* **64** 023607
- [43] Dalfovo F, Giorgini S, Pitaevskii L P and Stringari S 1999 *Rev. Mod. Phys.* **71** 463–512
- [44] Buggle C, Léonard J, von Klitzing W and Walraven J T M 2004 *Phys. Rev. Lett.* **93** 173202
- [45] O’Hara K M, Hemmer S L, Gehm M E, Granade S R and Thomas J E 2002 *Science* **298** 2179–2182
- [46] Joseph J A, Thomas J E, Kulkarni M and Abanov A G 2011 *Phys. Rev. Lett.* **106** 150401
- [47] Zwierlein M W, Abo-Shaeer J R, Schirotzek A, Schunck C H and Ketterle W 2005 *Nature* **435** 1047–1051
- [48] Schunck C H, Zwierlein M W, Schirotzek A and Ketterle W 2007 *Phys. Rev. Lett.* **98** 050404
- [49] Zhang W and Sá de Melo C A R 2007 *Phys. Rev. A* **76** 013627
- [50] Cederbaum L S, Streltsov A I, Band Y B and Alon O E 2007 *Phys. Rev. Lett.* **98** 110405
- [51] Xiong H, Liu S and Zhan M 2006 *New J. Phys.* **8** 245